



## RESEARCH ARTICLE

# Effect of boundary condition on the cyclic response of I-shaped steel columns: Two-story subassembly versus isolated column tests

Chung-Che Chou<sup>1,2</sup>  | Yun-Chuan Lai<sup>1</sup> | Hou-Chun Xiong<sup>1</sup> | Te-Hung Lin<sup>1,2</sup> |  
Chia-Ming Uang<sup>3</sup> | Gilberto Mosqueda<sup>3</sup> | Gulen Ozkula<sup>4</sup>  | Sherif El-Tawil<sup>5</sup> |  
Jason P. McCormick<sup>5</sup>

<sup>1</sup>Dept. of Civil Engineering, National Taiwan University, Taipei, Taiwan

<sup>2</sup>National Center for Research on Earthquake Engineering (NCREE), Taipei, Taiwan

<sup>3</sup>Dept. of Structural Engineering, University of California, San Diego, USA

<sup>4</sup>Dept. of Civil Engineering, Tekirdağ Namik Kemal University, Tekirdağ, Turkey

<sup>5</sup>Dept. of Civil and Environmental Engineering, University of Michigan, Ann Arbor, USA

## Correspondence

Chung-Che Chou, National Center for Research on Earthquake Engineering (NCREE), Taipei, Taiwan.  
Email: [cechou@ntu.edu.tw](mailto:cechou@ntu.edu.tw)

## Abstract

Recent studies on isolated steel columns under combined axial load and cyclic lateral drift showed that the column response is affected by the boundary condition. To consider more realistic boundary conditions of first-story columns in a frame, two-and-a-half story beam-column subassemblages were tested to investigate their behavior under reversed cyclic loading. The subassemblages, composed of a steel column with steel beams at two floor levels, used highly ductile I-shaped sections with web slenderness of either 37 or 49. Two isolated fixed-fixed columns were tested to facilitate a direct comparison with the subassembly testing. An axial compression force corresponding to 20% of the yield force was applied. Test results showed that the realistic boundary condition at the top end of the first-story column significantly alters the column plastic hinging, moment distribution, and out-of-plane deformation reported previously based on isolated column testing. Plastic hinging of the adjoining beams caused the inflection point of the first-story column to move upward initially, then moved downward when plastic hinging developed at the column base. Out-of-plane deformation observed from isolated columns did not occur in the subassembly column because hinging did not occur at the top end. Plastic components of the backbone curves for both the subassembly column and isolated column were very similar; the former delivered a larger story drift angle rotation due to a larger yield rotation, dependent on the elastic lateral stiffness of the column. A closed-form solution that calculates this stiffness for any boundary condition was developed and verified from test results.

## KEYWORDS

boundary condition, buckling, cyclic test, I-shaped column, inflection point, two-story subassembly frame

## 1 | INTRODUCTION

The axial force due to gravity and overturning forces in the first-story columns of medium-to-high rise buildings can adversely influence the members' flexural capacity and ductility under lateral drift. Although the strong-column/weak-beam concept is adopted in modern seismic design codes, plastic hinging and associated local buckling are expected to occur near the column base, which can influence the overall behavior of the system, including global stability.<sup>1</sup>

Driven by testing convenience and simplicity, it is common to investigate the seismic response of steel columns by conducting cyclic tests on isolated members with either a cantilever or fixed-fixed boundary condition.<sup>2–9</sup> Studies that employed fixed-fixed columns have generally shown that the column's seismic performance is strongly influenced by its local and global slenderness ratios, the level of axial force, and the material yield strength. Fixed-fixed boundary conditions imply that the inflection point is located at the mid-height of the column. In an actual moment frame system, the top end of a first-story column has some rotational flexibility given by the panel zone, beams and the second-story column. Therefore, a test setup with either a cantilever or fixed-fixed boundary condition, which does not allow the inflection point to move, cannot reflect the moment redistribution in the first-story columns in a multistory frame caused by plastic hinge formation at either the column base or ends of the beams framing into the top end of the column. To simulate a more realistic boundary condition at the top end of first-story columns experiencing double-curvature bending in an earthquake, cyclic response of two-and-a-half story beam-column subassemblages was investigated.

Recent studies have shown that the seismic performance of steel columns is affected by the boundary condition at both ends of the column. Elkady and Lignos<sup>7</sup> conducted tests on isolated columns with fixed-flexible and fixed-fixed boundary conditions. A predefined rotation mechanism was applied to the top end of the column specimens to simulate the flexible boundary condition. While specimens with both boundary conditions followed a similar damage progression, the story drift capacity was larger when the top end of the column was allowed to rotate. Thus, column specimens with a fixed-fixed boundary condition might not reflect the actual behavior of first-story columns in buildings. Wu et al.<sup>10</sup> conducted finite element analyses of deep wide-flange columns and showed that columns with a flexible-fixed boundary condition generally exhibited a larger drift capacity, 0.01 rad more than those with fixed-fixed boundary conditions.

To study the response of first-story columns in a frame, system-level testing in the form of either shake table testing<sup>11</sup> or hybrid testing<sup>12</sup> is ideal to reflect actual boundary conditions and internal force redistribution of a redundant steel building frame. Such testing has not been conducted to study deep columns to date, mainly due to the high cost involved at large-scale. Substructuring studies for hybrid testing have demonstrated more realistic boundary conditions on key members that can extend the specimen boundaries.<sup>13</sup> To supplement data from isolated column tests, an intermediate approach involving the use of a beam-column subassemblage was adopted in this research. Two half-scale subassemblage frame specimens were tested, each consisting of a two-story column with beams extending half of the bay width.<sup>14,15</sup> Parallel to this effort, two isolated columns of the same sizes were also tested to demonstrate and contrast the findings from subassemblage testing. The objectives of the paper are to (1) present test results of both the two-story steel subassemblages and isolated columns, (2) discuss the effect of boundary conditions on the column hysteretic response and buckling mode, and (3) quantify the influence of the top-end boundary condition on the cyclic backbone curves of first-story columns. Furthermore, the elastic stiffness for a relationship between the column base moment and the story drift angle for first-story columns in the frame was developed by considering the rotational flexibility at the column ends because it affects the yield rotation, which in turn affects the determination of the plastic rotation capacity of the columns.

## 2 | TEST SPECIMENS

The prototype structure is based on the design of a seven-story apartment building located in Taiwan.<sup>16</sup> The lateral force resisting frame is a dual system with a special moment frame (SMF) in one bay and a buckling-restrained braced frame (BRBF) in the other bay as shown in Figure 1(A). The two-and-a-half story subassemblage to be evaluated experimentally is also shown in Figure 1(A). The main focus of this research was to evaluate the seismic response of first-story columns with plastic hinging at the base while beams were also expected to form plastic hinges. The subassemblage was selected to provide realistic boundary condition at the top end of this column, by extending the column through the full-height of the second story and the mid-height (i.e., the assumed inflection point) of the third-story column. In addition, the adjoining beams were included at the second and third floors. The strong column-weak beam requirement was met in design such that no inelastic action was expected in the column above the first story.

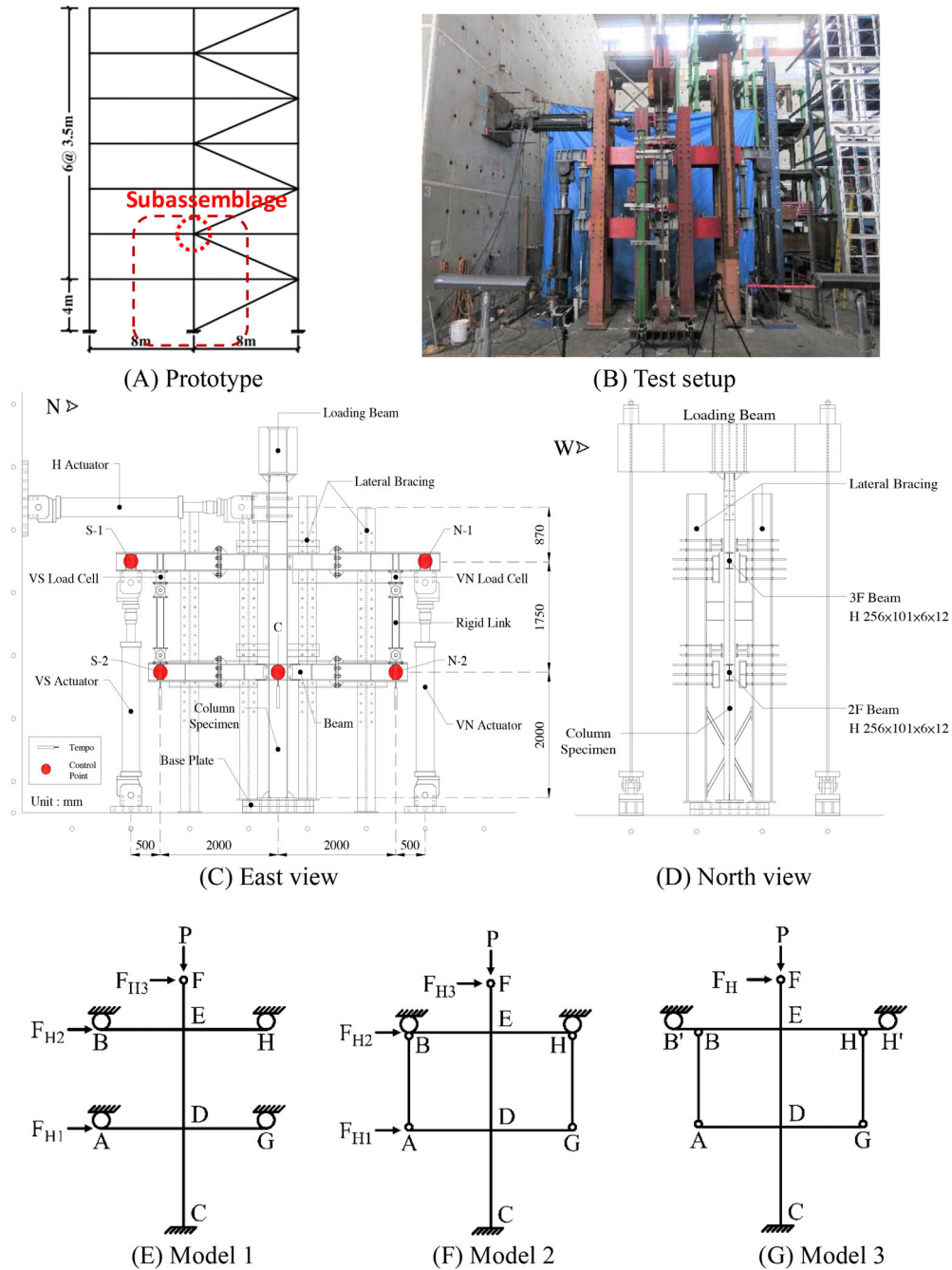


FIGURE 1 Prototype and subassembly test frame

Figure 1(B) to (D) show the experimental subassembly and the test setup. The length of each beam was half of the bay width, assuming the inflection point at the midspan; Figure 1(E) shows schematically the model of the subassembly. Note that the boundary condition at the beam inflection points (A, B, G, and H) allows for horizontal, but not vertical, movement, which is a reasonable assumption when column axial deformation is negligibly small.<sup>12</sup> Since four vertical reactions (i.e., beam shears) exist at these four locations, four vertical actuators would be required to apply these boundary forces. To simplify the test setup, it was decided to use rigid links AB and GH [Figure 1(F)] such that only two vertical actuators were needed to provide vertical reactions at B and H. In actual implementation, each vertical actuator needed to be offset horizontally from the nearby rigid link by a small distance in order to avoid conflict in the test setup [see Figure 1(C) and (G)].

Considering next the horizontal forces in the subassembly, a total of three applied forces ( $F_{H1}$ ,  $F_{H2}$ , and  $F_{H3}$ ) would be needed to simulate the force boundary conditions. To avoid using three horizontal actuators, another simplification

TABLE 1 Specimen dimension

	IC-37-S(R)	IC-37-I	IC-49-S	IC-49-I	Beam
	I-Shaped Column (IC-37)		I-Shaped Column (IC-49)		I-Shaped Beam
Section	320 × 160 × 8 × 12		320 × 160 × 6 × 12		256 × 101 × 6 × 12
$b_f/2t_f$	6.7	6.7	6.7	6.7	4.2
$h/t_w$	37	37	49	49	39
$L_b/r_y$	55	54	52	51	–

TABLE 2 Measured material properties

Section	Flange		Web	
	$F_y$ (MPa)	$F_u$ (MPa)	$F_y$ (MPa)	$F_u$ (MPa)
IC-37 Column	360	545	360	564
IC-49 Column	360	545	360	557
Beam	360	545	360	557

was again made by lumping all three forces at the column top ( $F$ ) as shown in Figure 1(G). Since the column shear would be the same in every story, one drawback of this approach is that the moments in the columns above the first story would be higher. A pre-test design check and the associated finite element simulation were conducted, and it was found that the portion of column above the first story would still remain elastic. Therefore, the boundary condition at the top end of the first-story column was judged to be still representative of the original intent.

Once plastic hinging occurs at the column base, significant shortening of the first-story column due to local or lateral buckling is expected to occur. The shortening would produce differential “settlement” of the beams due to the vertical restraint at B' and H' [Figure 1(G)]. Assuming that the test column represents an interior column and the neighboring columns would also perform similarly, then the “settlement” phenomenon would not occur. In this test program, the vertical displacements at locations B' and H' were made equal (or “slaved”) to that measured at location D.

The two subassemblages are designated as IC-37-S(R) and IC-49-S where the first two letters in the designation refer to the column type (I-I-shape and C-Column), the second values refer to the slenderness ratio of the columns web and the third set of letters refers to the type of test (S-subassembly and I-isolated). The (R) refers to the fact that the reported IC-37-S(R) specimen was the second test of this size due to friction concerns between the lateral bracing system and beams for the initial IC-37-S subassemblage. For all of the reported tests, Teflon pads were added at all interfaces between the lateral bracing system and the beams to minimize the friction. The columns and beams listed in Table 1 are built-up I-shaped members. The flange plates are connected to the web plate with complete-joint-penetration groove welds. SN490B steel with a nominal yield strength of 325 MPa was specified, and the measured mechanical properties are summarized in Table 2. The column size for Specimen IC-37-S(R) is a half-scale version of the prototype column H640×320×16×24[in mm], which is similar to the deep wide-flange shape of W24×131(622×316×15×24 in mm), representing a deep-column member size for SMFs. The column section of Specimen IC-49-S is the same as that of Specimen IC-37-S(R), except that the thickness of the web is reduced by 25% such that the effect of web slenderness ratio,  $h/t_w$ , could be evaluated in this study, where  $h$  is the clear distance between flanges when welds are used for the built-up section and  $t_w$  is the thickness of web. Table 1 also lists the section slenderness ratios ( $h/t_w$  for web local buckling and  $b_f/2t_f$  for flange local buckling) and member slenderness ratio ( $L_b/r_y$ ) of the columns, where  $b_f$  is the width of the flange,  $t_f$  is the thickness of the flange,  $L_b$  is the column clear length, and  $r_y$  is the radius of gyration about the y-axis (weak axis).

The column sections were designed to meet the highly ductile requirement in AISC 341-16.<sup>14</sup> For the flanges, the  $b_f/2t_f$  ratio is limited to

$$\lambda_{hd} = 0.32 \sqrt{\frac{E}{R_y F_y}} \quad (1)$$



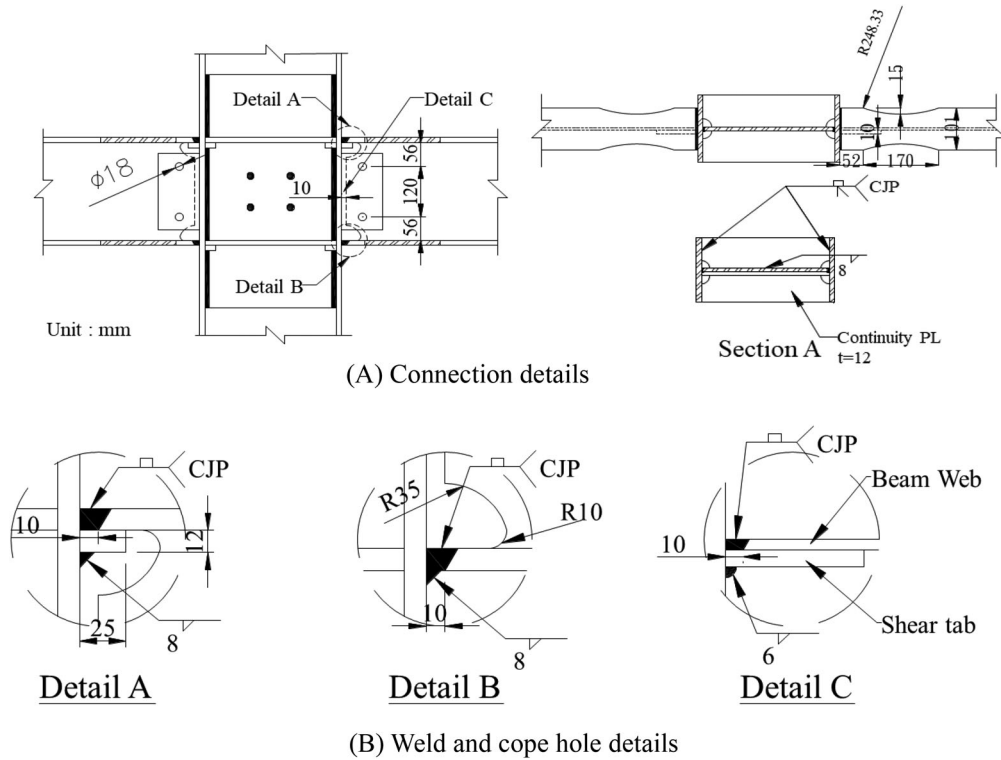


FIGURE 2 Subassemblage specimen connection details [Specimen IC-37-S(R)]

and for the web, the  $h/t_w$  ratio cannot be larger than the following when the axial load ratio,  $C_a$ , is larger than 0.114:

$$\lambda_{hd} = 0.88 \sqrt{\frac{E}{R_y F_y}} (2.68 - C_a) \geq 1.57 \sqrt{\frac{E}{R_y F_y}} \quad (2)$$

where

$$C_a = \frac{P_u}{0.9 R_y F_y A} \quad (3)$$

In this test program, the value of  $C_a$  was taken as 0.2. Together with  $F_y = 325$  MPa and  $R_y = 1.1$ , the  $\lambda_{hd}$  values equal 7.5 and 51.6 for the flanges and web of the columns, respectively. The  $b_f/2t_f$  and  $h/t_w$  ratios listed in Table 1 show that columns in the subassemblage specimens met this requirement. The H256×101×6×12 [in mm] beams also met the highly ductile requirement.<sup>17</sup>

It is commonly assumed in the design of SMF that column bases are fixed. To achieve this boundary condition as practical as possible, a thick ( $t = 40$  mm) base plate was used. To minimize potential bending of the base plate, stiffeners were also added [Figure 1(C)]; adding stiffeners also eliminated the potential fracture of CJP welds between the column and base plate, a failure mode that was not the focus of this study. Although this “near fixed” boundary condition may not reflect that in real construction, it eliminated the uncertainty on elastic stiffness prediction to be presented in Section 5. The presence of these stiffeners was not expected to influence local buckling of the column, although the plastic hinge location might be shifted upward by a small amount. A Reduced Beam Section (RBS) moment connection based on AISC 358<sup>18</sup> was used for connecting the beams to the column. The geometry of the RBS together with the connection details for Specimen IC-37-S(R) is provided in Figure 2. A 10-mm thick doubler plate was used to meet the panel zone strength requirement. The strong column/weak beam concept was adopted for design of two specimens (1.53 and 1.44 for Specimens IC-37-S(R) and IC-49-S, respectively). Following fabrication practices in Taiwan, the beam web weld access hole was made by punching two small circles with radii of 35 and 10 mm, respectively. To explore the influence of boundary conditions, two isolated column specimens (IC-37-I and IC-49-I) were also fabricated. As indicated in Table 1, these specimens have the same column sections and lengths as the subassemblages, IC-37-S(R) and IC-49-S, respectively.

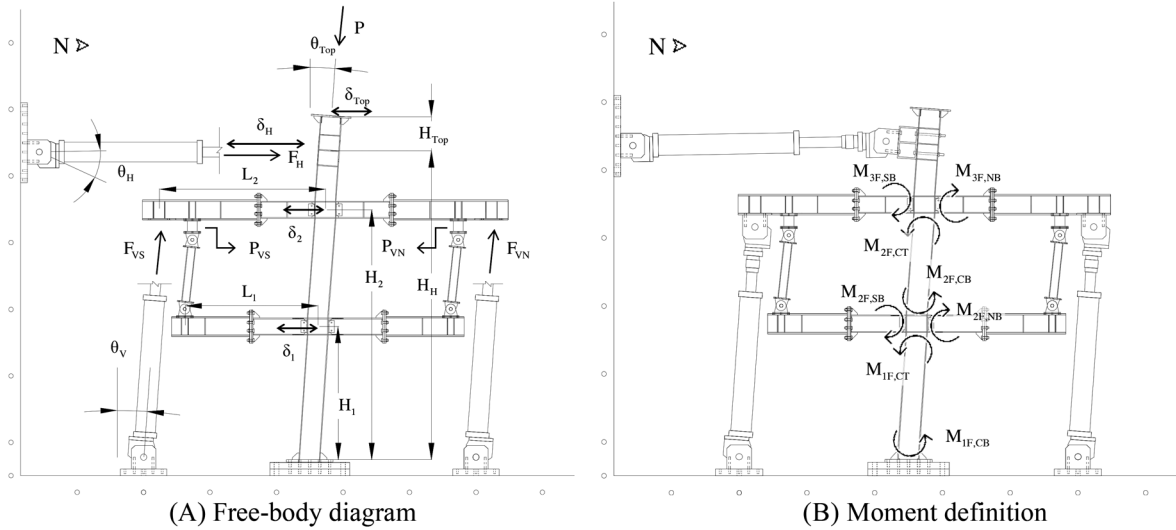


FIGURE 3 Freebody diagram and moment definition for the subassembly specimens

### 3 | TEST SETUP AND DATA REDUCTION

#### 3.1 | Subassembly frames

The test setup for the subassembly testing is shown in Figure 1. BRBs are expected to induce large and alternating axial loads in the BRBF columns. To simplify the test setup, BRBs were not included in the subassembly tests. Instead, a constant axial load was applied to the column. These simplifications led to a first-story column which is more representative of that in an SMF. Therefore, the cyclic loading history specified in AISC 341<sup>17</sup> for SMF connection testing, not for BRBF testing, was used in this test program. A constant axial load,  $P$ , corresponding to  $C_a = 0.2$  was applied to the top end of the column via a stiff loading beam, hydraulic jacks, and post-tensioned bars [see Figure 1(D)]. To simplify the test setup, only one horizontal actuator was attached to the top end of the column to simulate seismic loading. The imposed horizontal displacement and the measured horizontal force are designated as  $\delta_H$  and  $F_H$  in Figure 3(A). Therefore, the column (or story) shear is the same in the first and second stories. The inflection point of each beam in the third floor was simulated by connecting a vertical actuator at the free end of each beam; the measured vertical actuator forces [ $F_{VS}$  and  $F_{VN}$  in Figure 3(A)] were used to compute the beam shears. To overcome the challenge of installing another two vertical actuators for the second-floor beams due to limited space, two pin-ended rigid links were used to model constant floor spacing since the second-story column was not expected to shorten. Forces measured by the load cell installed at the top end of each link [ $P_{VS}$  and  $P_{VN}$  in Figure 3(A)] were then used to determine the beam shears in the second floor. Axial shortening of the first-story column was expected during testing. Assuming that all first-story columns would also shorten by the same amount, the measured vertical displacement at the second-floor panel zone location was used as the feedback to control two vertical actuators such that the cantilevered ends of all four beams would displace downward by the same amount. The test was conducted pseudo-statically with an actuator velocity of 2 mm/s, and the measurement of the vertical displacement of the second-floor panel zone [point C in Figure 1(C)] was a command value to control the two vertical actuators. The control system commanded the actuators with a frequency of 2048 Hz. The accuracy of the displacement command was controlled within 0.05 mm. Therefore, the column axial shortening reflected by the command/response delay of the vertical actuator control was minimal.

Based on the free-body diagram in Figure 3(A), the following column end moments shown in Figure 3(B) can be established from the measurements:

$$\begin{aligned}
 M_{1F,CB} = & [H_H F_H \cos \theta_H - (H_H + H_{Top}) P \sin \theta_{Top}] \\
 & + [P \cos \theta_{Top} \delta_{Top} + F_H \sin \theta_H \delta_H] \\
 & + [(F_{VS} - F_{VN}) L_2 \cos \theta_V + (F_{VS} + F_{VN}) H_2 \sin \theta_V]
 \end{aligned} \quad (4)$$

$$M_{1F,CT} = [(H_H - H_1 + 0.5d_B)F_H \cos\theta_H - (H_H + H_{Top} - H_1 + 0.5d_B)P \sin\theta_{Top}] + [P \cos\theta_{Top} (\delta_{Top} - \delta_1) + F_H \sin\theta_H (\delta_H - \delta_1)] \quad (5)$$

$$M_{2F,CB} = [(H_H - H_1 - 0.5d_B)F_H \cos\theta_H - (H_H + H_{Top} - H_1 - 0.5d_B)P \sin\theta_{Top}] + [P \cos\theta_{Top} (\delta_{Top} - \delta_1) + F_H \sin\theta_H (\delta_H - \delta_1)] + [(F_{VS} - F_{VN})L_2 \cos\theta_V + (F_{VS} + F_{VN})(H_2 - H_1 + 0.5B) \sin\theta_V] + (P_{VS} - P_{VN})L_1 \quad (6)$$

$$M_{2F,CT} = [(H_H - H_2 + 0.5d_B)F_H \cos\theta_H - (H_H + H_{Top} - H_2 + 0.5d_B)P \sin\theta_{Top}] + [P \cos\theta_{Top} (\delta_{Top} - \delta_2) + F_H \sin\theta_H (\delta_H - \delta_2)] + [(F_{VS} - F_{VN})L_2 \cos\theta_V + (F_{VS} + F_{VN})(H_H - H_2 + 0.5B) \sin\theta_V] + (P_{VS} - P_{VN})L_1 \quad (7)$$

where  $\theta_v$  is the inclination angle of the vertical actuators, and  $\theta_{Top}$  is the frame drift angle:

$$\theta_{TOP} = \frac{\delta_H}{H_H} \quad (8)$$

where  $\delta_H$  is the corresponding top-end horizontal displacement of the column in the subassembly frame when the first-story drift angle follows the AISC loading sequence for testing beam-to-column moment connections.<sup>14</sup>

The following beam moments at the column face are calculated from the measured vertical actuator forces,  $F_{VS}$  and  $F_{VN}$ , and the axial forces in the rigid links,  $P_{VS}$  and  $P_{VN}$ :

$$M_{2F,SB} = [P_{VS} (L_1 - 0.5d_C)] \quad (9)$$

$$M_{2F,NB} = [P_{VN} (L_1 - 0.5d_C)] \quad (10)$$

$$M_{3F,SB} = [F_{VS} (L_2 - 0.5d_C) \cos\theta_V - M_{2F,SB}] \quad (11)$$

$$M_{3F,NB} = [F_{VN} (L_2 - 0.5d_C) \cos\theta_V - M_{2F,NB}] \quad (12)$$

where  $d_C$  is the column depth. Each subassembly frame was tested pseudo-statically by imposing a pre-defined displacement history of  $\delta_H$  to the top end of the column [see Figure 4(A)].

### 3.2 | Isolated columns

Two isolated columns (Specimens IC-37-I and IC-49-I) were tested by using the Multi-Axial Testing System (MATS) at the NCREC laboratory. MATS can impose both axial compression and cyclic lateral drifts to the specimens. The measured first-story drift angle from each subassembly test was imposed to the corresponding isolated column specimen by displacing horizontally one end of the column relative to the other [see Figure 4(B)].

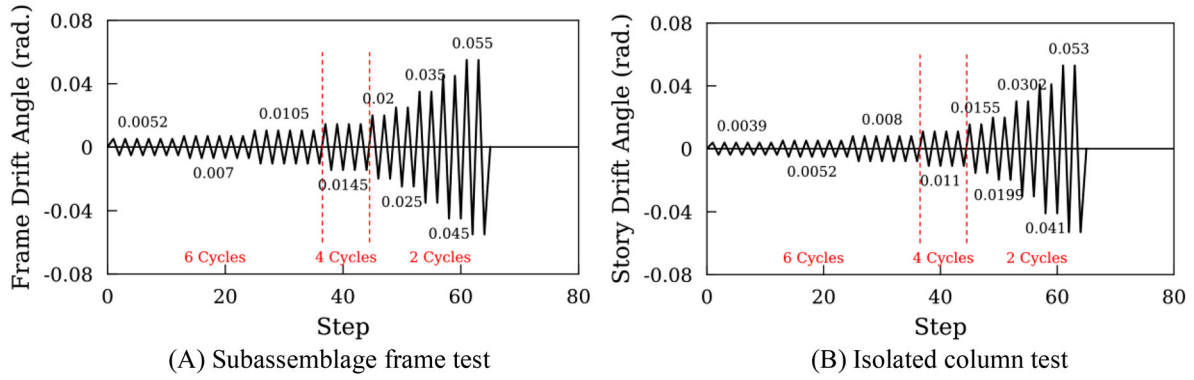


FIGURE 4 Displacement protocols for subassembly frame and column tests

### 3.3 | Experimental results of subassembly frame tests

The first- and second-story drift angles are defined as the relative lateral displacement divided by the respective column heights, 2000 and 1750 mm [Figure 1(C)], and the overall frame drift angle is defined in Equation (8). The beam end moment is normalized by the plastic moment,  $M_p = ZF_y$ , where  $Z$  is the plastic section modulus about the major axis of bending, and  $F_y$  is the measured yield stress listed in Table 2. The column end moment is normalized by the reduced plastic moment,  $M_y$ :

$$M_y = \frac{9}{8}M_p \left(1 - \frac{P}{P_y}\right) \quad (13)$$

where  $P_y$  is the axial yield force of the column based on the measured yield stress (Table 2).

#### 3.3.1 | Specimen IC-37-S(R)

Figure 5(A) and (B) show the response plots of both the horizontal actuator force and the column axial force versus the frame drift angle, respectively. The specimen started to show yielding at the column base and beam flanges when the frame drift angle reached 0.0105 rad. Local buckling was observed in the beam webs and flanges at a frame drift angle of 0.02 rad. Column local buckling was also visible near the base at 0.025 rad, where the buckling amplitudes in the north and south flanges reached 4 and 9 mm, respectively, and the web buckling amplitude was about 1 mm. The specimen developed a peak strength at 0.035 rad before it started to degrade due to significant local buckling near the column base. Each column flange buckled in an antisymmetric manner with respect to the column web, i.e., the Antisymmetric Local Buckling (ALB) as classified by Ozkula et al.<sup>16</sup> Local buckling amplitudes increased significantly at higher drift levels (Figure 6). At 0.045 rad, the maximum amplitude in the flanges reached 107 mm, and severe local buckling in the web also occurred (37 mm), which was accompanied by a significant shortening (47 mm) in the column [Figure 7(A)].

Figure 8(A) to (D) show the response plots of the columns in the first and second stories. It is observed that the moment at the bottom of each column was larger than that at the top, indicating that the inflection point was above the mid-height of the column. The strength degradation due to local buckling at the column base after reaching the peak strength is obvious from Figure 8(A). Figure 8(C) also shows strength degradation during the second cycle at 0.055 rad drift. The strength degradation of the two-story subassembly frame specimen [Figure 8(A)] is first caused by the plastic hinge formation near the column base [Figure 6(A)], and then by the fracture of the north beam flange at the second floor [Figure 8(F) and Figure 9(C)]. Note that the fracture occurring near the beam flange CJP weld was also reported by Reynolds and Uang.<sup>20</sup> If the first-story column response at the base is only considered [Figure 8(A)], the column fails to maintain 90% of the maximum flexural strength after the first-story drift angle reached 0.03 rad. Note that the so called “significant” strength degradation in both the first-story column [Figure 8(A)] and the 2F north beam fracture [Figure 5(C) and Figure 8(F)] has been “smeared” at the global response level [Figure 5(A)], i.e., the system strength degradation is much less than the

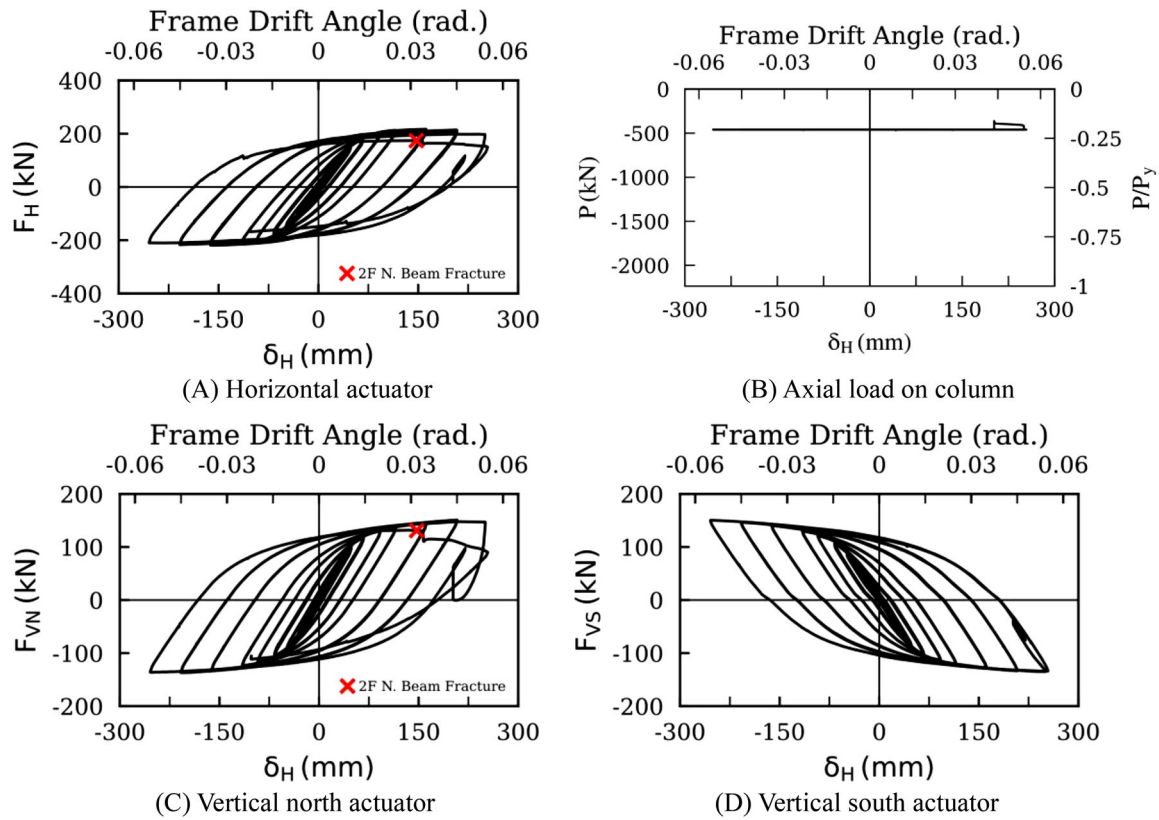


FIGURE 5 Specimen IC-37-S(R) response

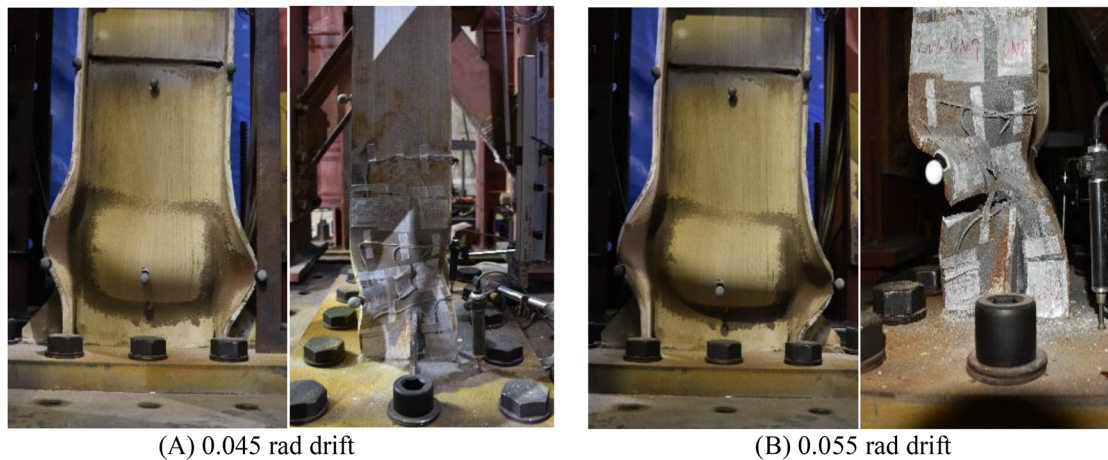


FIGURE 6 Column buckling in Specimen IC-37-S(R)

member strength degradation. No yielding or buckling was found at the top end of the first-story column throughout the test.

The same size beams were used in the second and third floors. Because the lateral load was applied at the top end of the subassembly, it was expected that the behavior of all four beams would be similar [Figure 8(E) to (H)] because the column (or story) shear was the same in each story. Flange and web local buckling in the beams was visible at 0.025 rad drift. This local buckling was accompanied by lateral torsional buckling at higher drifts [Figure 9(A)]. The bottom flange of the north beam in the second floor fractured during the second cycle at 0.055 rad drift [Figure 9(C)].



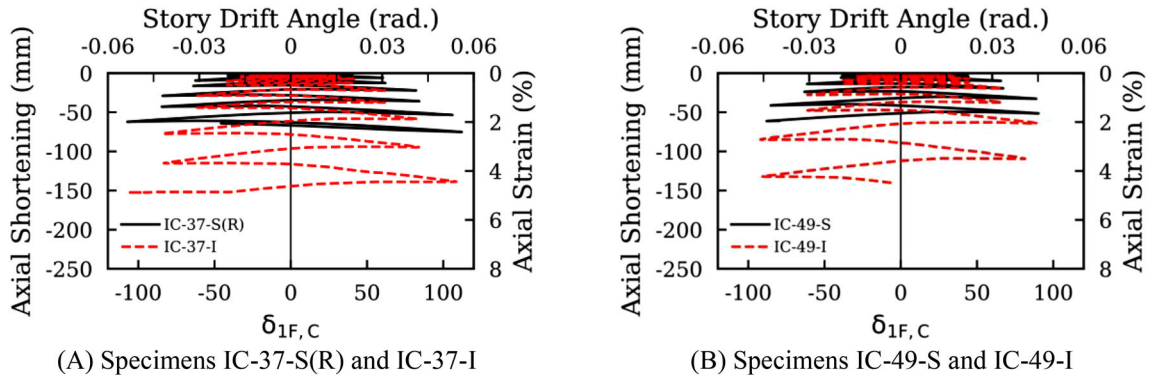


FIGURE 7 Column axial shortening

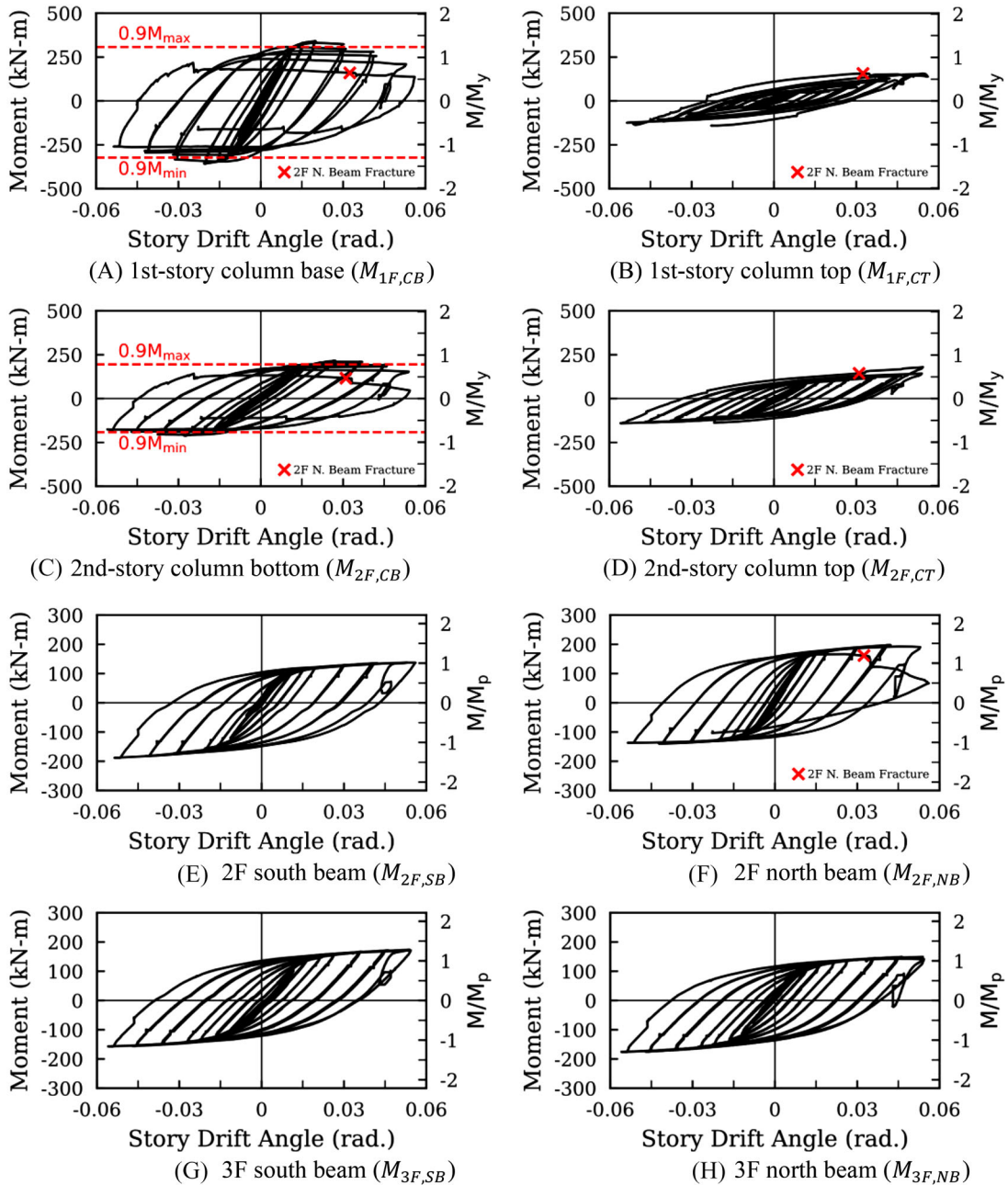


FIGURE 8 Moment response in Specimen IC-37-S(R)

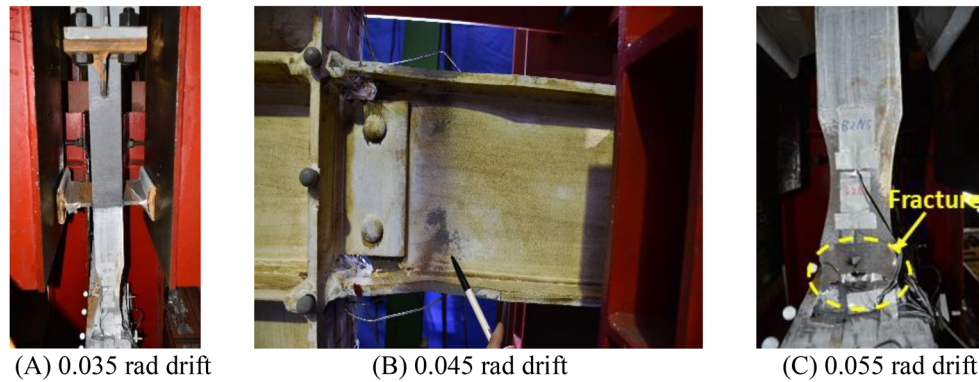


FIGURE 9 Beam buckling and fracture in Specimen IC-37-S(R)

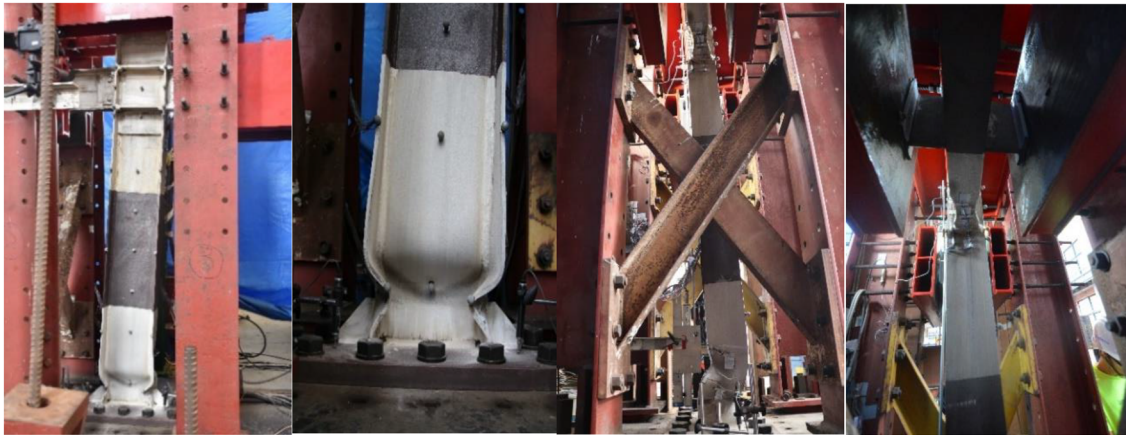


FIGURE 10 Observed response of Specimen IC-49-S (0.045 rad drift)

### 3.3.2 | Specimen IC-49-S

Specimen IC-49-S behaved similarly to Specimen IC-37-S(R) up to a frame drift angle of 0.0145 rad. Web local buckling was visible near the column base at 0.02 rad drift. The subassembly developed a peak strength during the first cycle to a frame drift angle of 0.025 rad, where the buckling amplitudes in the column north and south flanges reached 11 mm and the column web buckling amplitude was 10 mm. At this drift level, the web buckling amplitude was much more significant in Specimen IC-49-S than in Specimen IC-37-S(R) because of the less compact column web plate of the IC-49-S. Each column flange also buckled in an antisymmetric manner with respect to the column web, similar to Specimen IC-37-S(R). At 0.045 rad drift, the buckling amplitudes in the north and south flanges at the base of the column reached 75 and 85 mm, respectively, and the column web buckling amplitude was approximately 60 mm.

Plastic hinge formation at the column base was accompanied by significant web buckling, causing the column to displace transversely between the column base to the 2F beam (Figure 10). The subassembly strength decreased more than 10% at 0.045 rad drift [Figure 11(A)], and the test was stopped after completing two cycles at this drift level due to significant local buckling near the column base (Figure 10). The moment at the column base started to decrease after the first-story drift angle reached 0.02 rad [Figure 11(B)] and it was noted that the strength degradation of Specimen IC-49-S at the column base was faster than that of Specimen IC-37-S(R) due to the more slender column web plate. No strength degradation was observed in the hysteresis response of the beams [Figure 11(C) to (D)], and no weld or plate fractures in the connections and beams were identified in post-test inspections. Note that the “significant” strength degradation at the column member level [Figure 11(B)] had also been “smeared” at the global response level [Figure 11(A)].

Considering the unavoidable geometric imperfections of the beams and columns, fit-up and welding effect during fabrication, it is practically not possible to fabricate a “planar” subassembly specimen. Prior to testing, the lateral bracing system was adjusted to accommodate any skew, i.e., out-of-plane alignment, of the beams. Although Teflon pads were

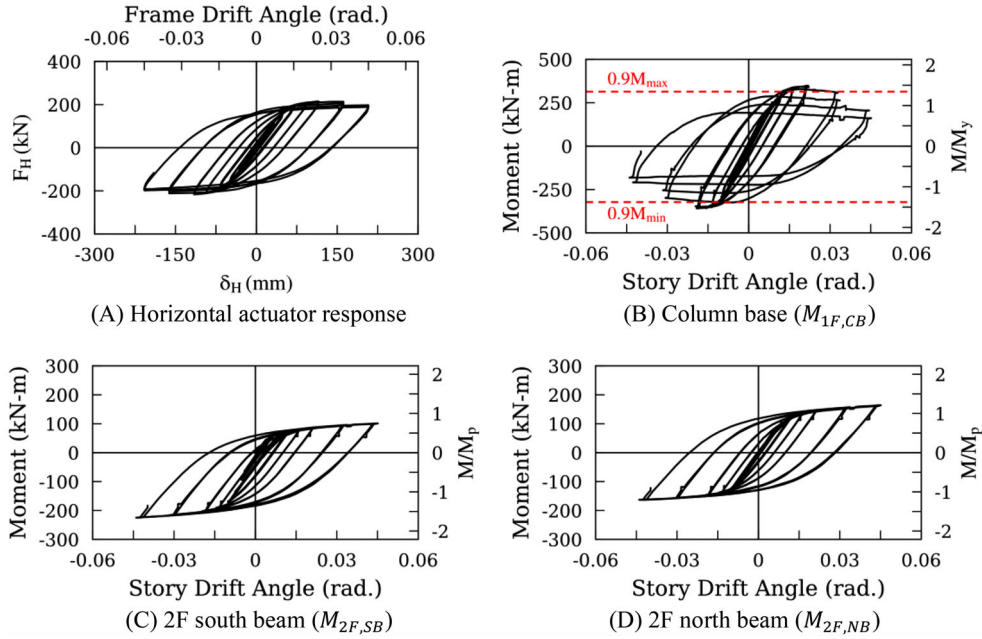


FIGURE 11 Moment response in Specimen IC-49-S

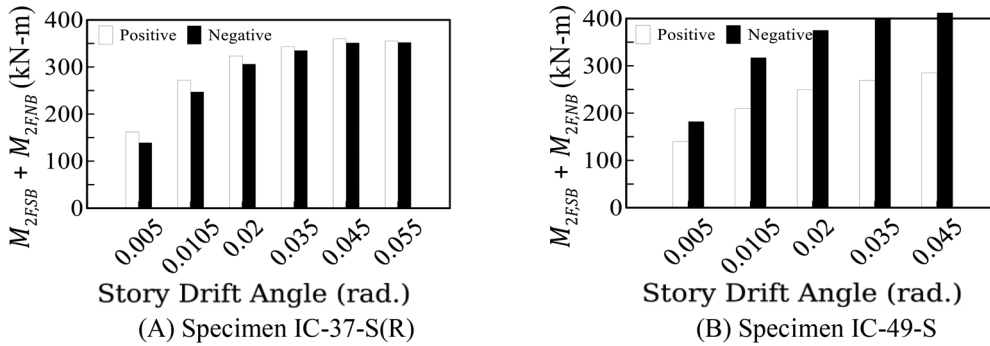


FIGURE 12 Unbalanced moment on the top of the first-story column

added to the interfaces between the bracing system and the beams to minimize the friction, eliminating it was not possible. The friction force would affect the measured forces of two vertical actuators ( $F_{VS}$  and  $F_{VN}$ ) and two vertical load cells ( $P_{VS}$  and  $P_{VN}$ ) as shown in Figure 3. It was expected that the friction would occur in one loading direction when the beam bear against the bracing system, but a separation would occur when the direction of loading was reversed. Since these four forces were used to calculate the beam moments and yet the friction forces were not measured, a close examination of Figure 8(E) shows that, for Specimen IC-37-S(R), the end moment of 2F south beam was larger in the negative drift direction than that in the positive direction. Similarly, Figure 8(F) shows the opposite trend for the 2F north beam. Since the summation of end moments of these two beams ( $= M_{2F,SB} + M_{2F,NB}$ ) represents the unbalanced beam moment applied to the top end of the first-story column, the unbalanced moment in Figure 12(A) shows that the unsymmetric effect from each beam end moment was greatly reduced; Figure 8(A) to (D) also shows that the effect of skew had a little effect on the responses of the first-story and second-story column. For Specimen IC-49-S, however, the unsymmetric nature of the 2F south beam moment in both drift directions was more significant [see Figure 11(C)], which was probably due to a larger skew in the fabricated specimen. Figure 12(B) shows that the unbalanced beam moment in the negative drift direction was about 49% larger than that in the other drift direction. But the first-story column response plot in Figure 11(B) shows that such effect would only increase the negative peak column base moment by 3%. Therefore, it is believed that the unintended, unsymmetric nature of the 2F south beam response had a small effect, and it was judged that it would not affect the observed behavior and overall response of the first-story column.



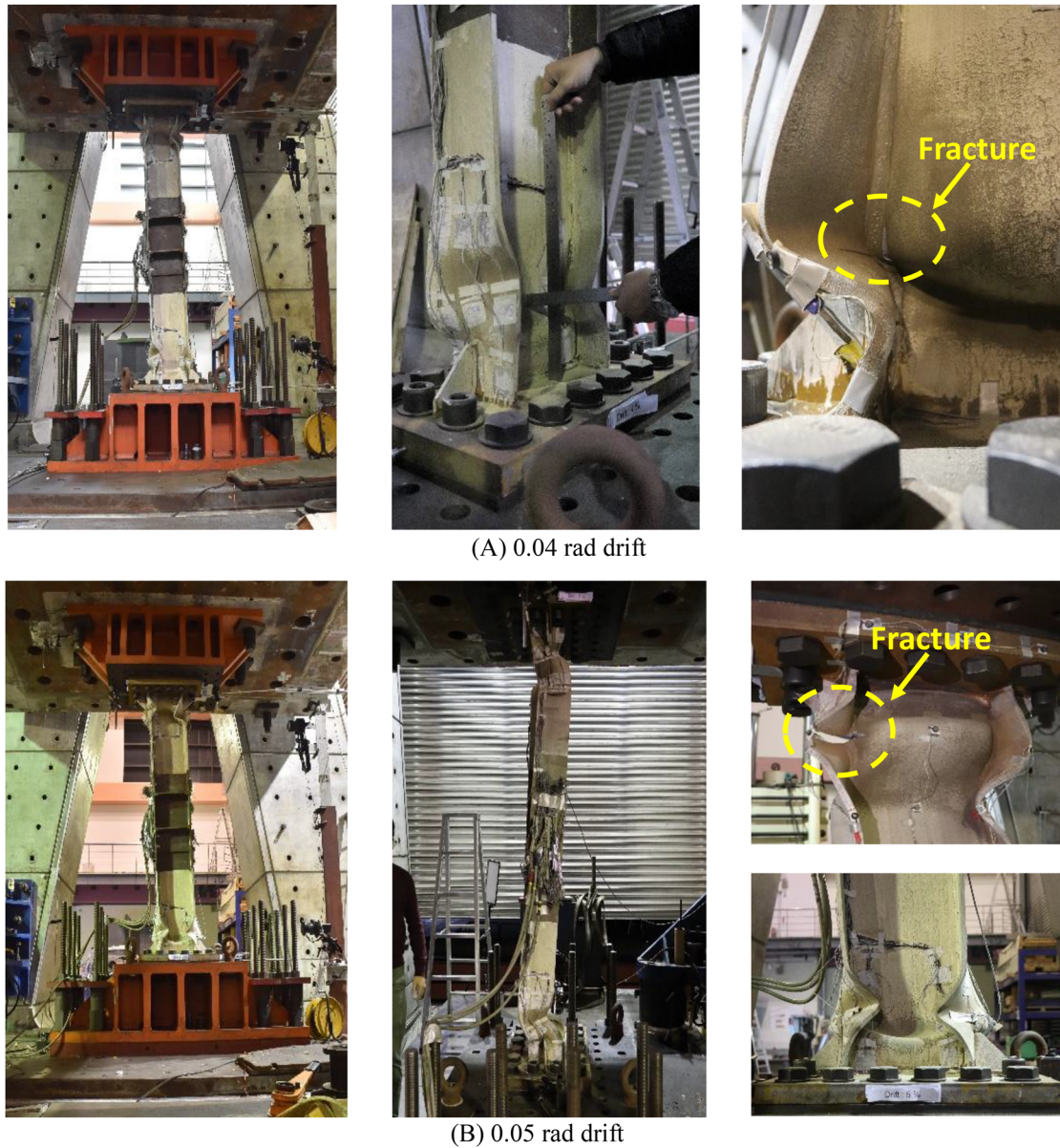


FIGURE 13 Observed performance of Specimen IC-37-I

### 3.4 | Experimental results of isolated column tests

#### 3.4.1 | Specimens IC-37-I and IC-49-I

Since strain gage measurements showed that the subassembly frame columns between the mid-height of the first story and second story remained essentially elastic during the tests, a length ( $l = 1972$  mm) above the mid-height of the first-story column was cut out for isolated column tests. The adjoining beams were removed, but continuity plates and doubler plate in the panel zone remained. Because these stiffening plates were located at the midheight (i.e., elastic portion) of the isolated columns, their presence was not expected to influence the column response. The measured first-story drift angles from the subassembly tests were imposed to the bottom (i.e., moving) end of the isolated columns.

The behavior of both column specimens (IC-37-I and IC-49-I) was similar. Figures 13 and 14 show plastic hinge formation at both ends of the columns. For Specimen IC-37-I ( $h/t_w = 37$ ), visible local buckling occurred at 0.015 rad, earlier than that observed in the subassembly frame [Specimen IC-37-S(R)] test. Peak strength was also reached earlier (at 0.02 rad drift). The local buckling amplitudes in the flanges and web were about 24 mm. The observed antisymmetric local buckling mode

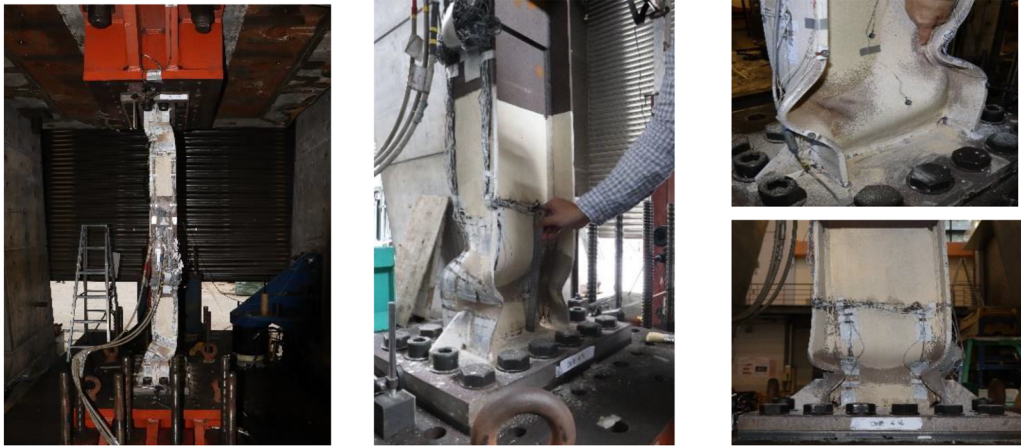


FIGURE 14 Observed performance of IC-49-I (0.04 rad drift)

was the same as that of Specimen IC-37-S(R). Specimen IC-37-I had a strength degradation of more than 20% at 0.03 rad drift. At 0.04 rad drift, the buckling amplitude in the flanges reached 67 mm, and significant local buckling in the web also occurred (62 mm). A groove weld connecting the web and the flange fractured at the bottom end at 0.04 rad drift level [Figure 13(A)]. Severe local buckling not only caused significant strength degradation but also led to fracture of the column flange at the top end of the column during the first cycle at 0.05 rad drift [Figure 13(B)]. Severe local buckling also caused both ends of the column to move transversely in the opposite direction.

Specimen IC-49-I ( $h/t_w = 49$ ) reached a peak strength at 0.02 rad drift and had a strength degradation of more than 20% at 0.03 rad drift. The buckling amplitude in the flanges and web was approximately 65 mm at 0.04 rad drift (Figure 14), and a crack was observed near the web-to-flange weld junction. The test was stopped after completing two cycles to 0.04 rad drift because the strength had degraded by more than 50%. Severe local buckling also caused both ends of the column to displace transversely, but in the same direction.

## 4 | EFFECT OF BOUNDARY CONDITION ON THE COLUMN RESPONSE

### 4.1 | Overall response

Specimens IC-37-S(R) and IC-37-I were tested with actual and fixed-fixed boundary conditions, respectively. Figure 15(A) shows the hysteretic response at the column base of the first-story column. Both the elastic flexural stiffness and the maximum strength of Specimen IC-37-I are higher than those of Specimen IC-37-S(R). However, the lateral strength of Specimen IC-37-I degrades faster than that of Specimen IC-37-S(R). A similar behavior is also observed when comparing Specimens IC-49-S and IC-49-I [Figure 15(B)]. Although the column web thickness of the two specimen pairs differs by 25% (i.e.,  $h/t_w$  ratios of 37 versus 49), the hysteretic response of both first-story columns is similar up to 0.03 rad drift for all four tests [Figure 15(C) and (D)]. However, the columns with thinner webs degraded faster than those with a thicker web in both test schemes.

To study the column moment distribution in the subassembly frame, the moment backbone curves obtained by connecting the peak positive moments at the first cycle of each drift are constructed at the column base,  $M_{IF,CB}$ , the first-story column top end,  $M_{IF,CT}$ , the second-story column bottom end,  $M_{2F,CB}$ , and the second-story column top end,  $M_{2F,CT}$ , as shown in Figure 16(A) and (B). Three steps representing the onset of member yielding (Steps 1-1, 1-2, and 1-3 in Table 3), the maximum strength (Step 2), and 90% of the maximum strength (Step 3) are marked in the  $M_{IF,CB}$  curve. Since the strong column-weak beam ratios are 1.53 and 1.44 for Specimens IC-37-S(R) and IC-49-S, respectively, beam yielding generally occurs earlier than column base yielding. After the column base yields, the moment at the column base increases with drift up to the maximum strength level (Step 2), but the moment at the first-story column top end,  $M_{IF,CT}$ , keeps constant with increasing drift, leading to a moment increase at the second-story column bottom end,  $M_{2F,CB}$ , associated with additional moment from the 2F beam plastic hinges. When local buckling at the column base becomes severe after the maximum strength level is reached (Step 2), the moment at the base starts to decrease and the moment at the first-story column top end,  $M_{IF,CT}$ , increases. The moment at the second-story column bottom end,  $M_{2F,CB}$ , also decreases with drift



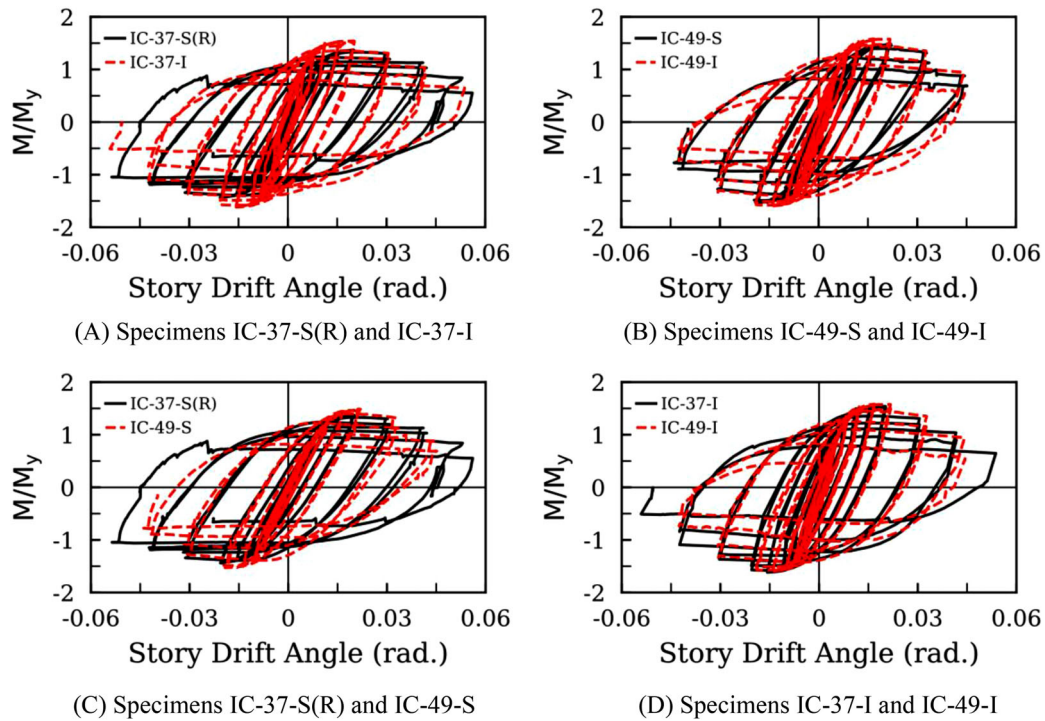


FIGURE 15 Hysteresis comparison between subassemblage and isolated columns

TABLE 3 Response progress in the subassemblage frame test

Damage State	Description
1-1	Onset of column yielding
1-2	Onset of second-floor (2F) beam yielding
1-3	Onset of third-floor (3F) beam yielding
2	Maximum moment at column base
3	10% reduction from maximum moment at column base

TABLE 4 Specimen response

Specimen	$M_y$ (kN-m)	$M_{max}^+$ (kN-m)	$\theta_y^+$ (rad.)	$\theta_{u,90\%}^+$ (rad.)	$\theta_{pu,90\%}^+$ (rad.)	$\theta_{u,80\%}^+$ (rad.)	$\theta_{pu,80\%}^+$ (rad.)
IC-37-S(R)	248	341	0.0092	0.0342	0.0250	0.0422	0.0330
IC-37-I	248	382	0.0049	0.0271	0.0221	0.0337	0.0288
IC-49-S	234	348	0.0085	0.0310	0.0225	0.0360	0.0275
IC-49-I	234	370	0.0056	0.0292	0.0236	0.0352	0.0296

+: mean positive direction.

after the maximum strength level is reached. Note that the moment at the bottom end of the second-story column,  $M_{2F,CB}$ , was close to reaching the reduced plastic moment,  $M_y$  [Equation (13)], at Step 2. The backbone curves of Specimens IC-37-I and IC-49-I are plotted in Figure 16(C) and (D), respectively, and show member yielding, maximum strength, and strength degradation at earlier drift levels than those of the subassemblage frame counterpart.

## 4.2 | Plastic rotation capacity

Table 4 lists the maximum moment,  $M_{max}$ , the yield rotation,  $\theta_y$ , corresponding to  $M_y$ , and the ultimate rotation,  $\theta_{u,90\%}$  and  $\theta_{u,80\%}$ , when the column moment decreases to 90% and 80% of  $M_{max}$ , respectively. Subtracting  $\theta_y$  from  $\theta_{u,90\%}$  and  $\theta_{u,80\%}$  gives the plastic rotation capacities,  $\theta_{pu,90\%}$  and  $\theta_{pu,80\%}$ . The column yield rotation,  $\theta_y$ , in the subassemblage frame

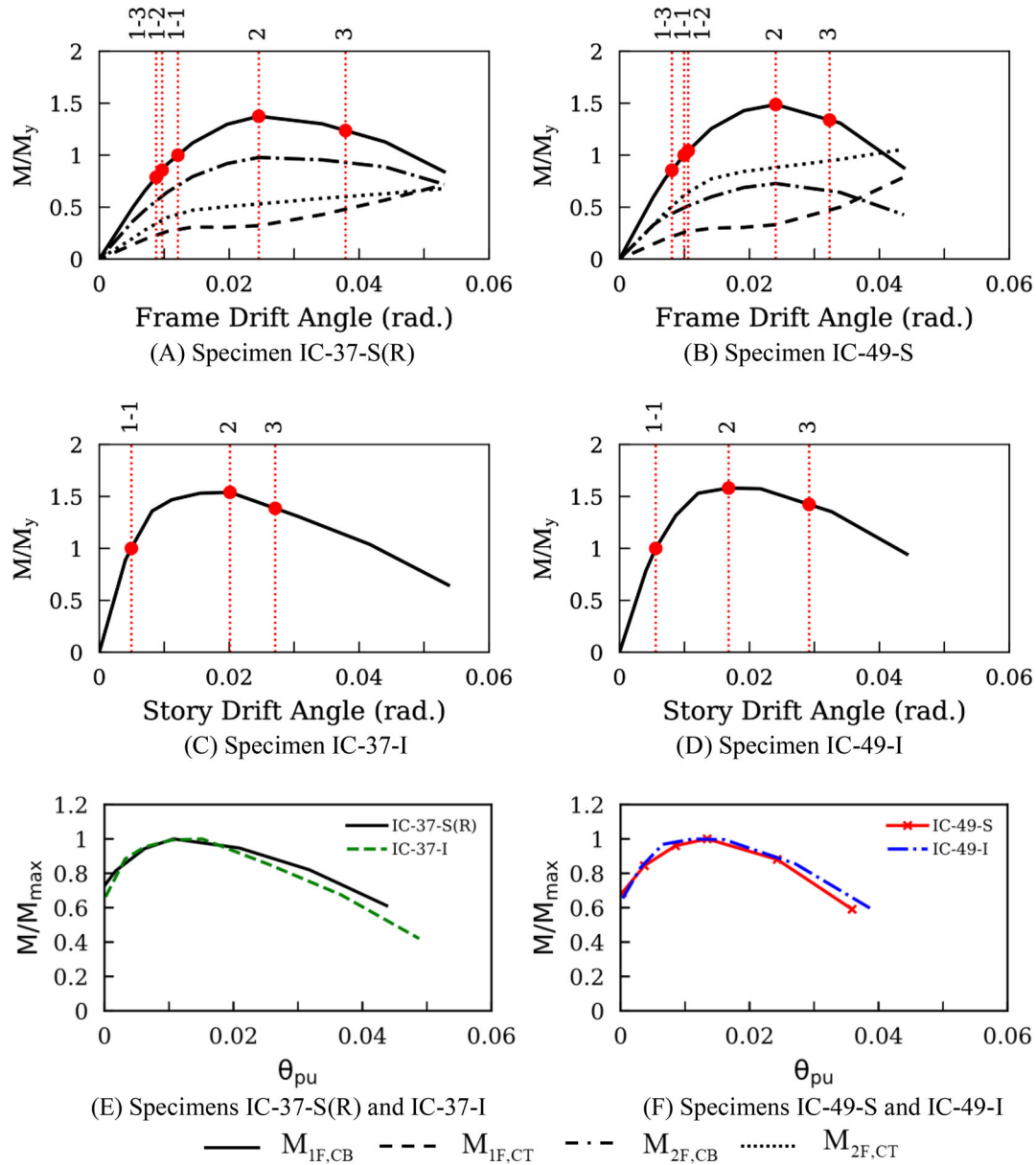


FIGURE 16 Backbone curves of column moment response

is significantly larger than its isolated counterpart with a fixed-fixed boundary condition. However, the plastic rotation capacity,  $\theta_{pu,90\%}$  or  $\theta_{pu,80\%}$ , is similar in each pair of specimens with the same web thickness [see Figure 16(E) and (F)].

### 4.3 | Inflection point location

The moment diagram along the column height is plotted at three different drift angles in Figure 17. For Specimen IC-37-S(R) in the elastic range (i.e., 0.007 rad drift), the inflection points of the first-story and second-story columns are located at 0.77 and 0.63 times the respective column heights [Figure 17(A)]. The inflection point of the second-story column is closer to the mid-height because this column has similar boundary condition at both ends. The inflection point of the first-story column first moves upward when beam hinging occurs until the maximum strength at the column base is reached. Then, the inflection point moves downward in the first- and second-story columns due to local buckling at the column base. However, the inflection point always remains at the mid-height for the isolated columns [Figure 17(C) and (D)].

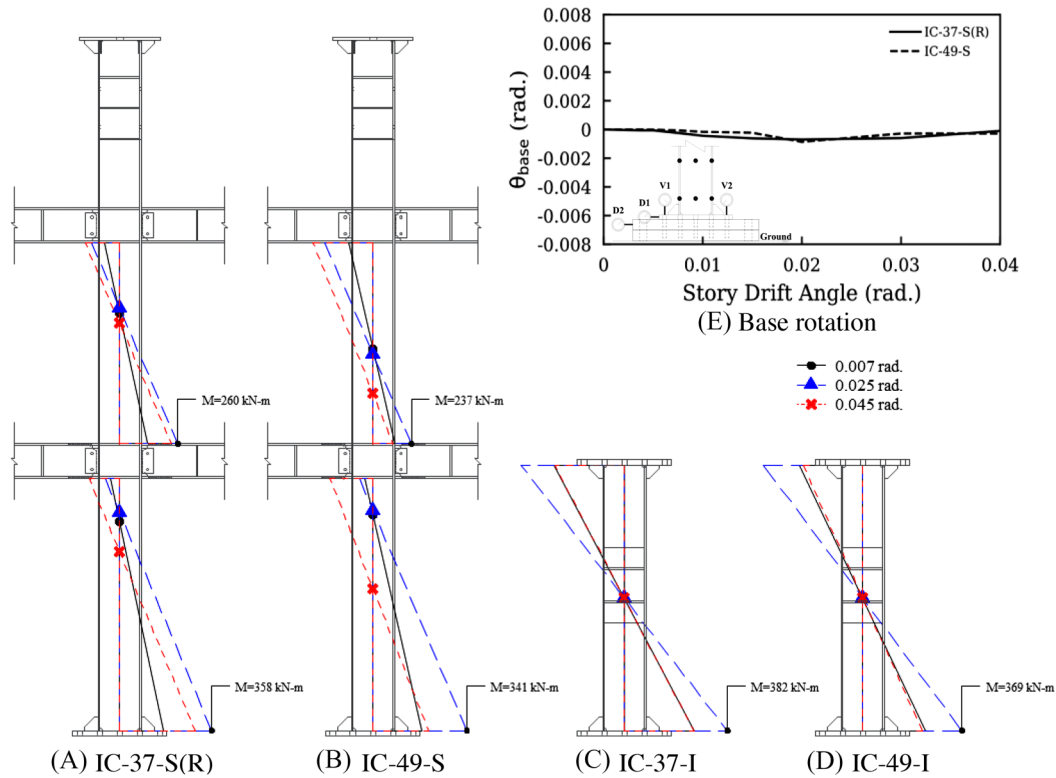


FIGURE 17 Inflection point variation in all specimens

#### 4.4 | Axial behavior

All four specimens tested were able to maintain their axial load capacity to a drift level of 0.04 rad, regardless of their boundary conditions. This result is consistent with findings by Wu et al.<sup>10</sup> who showed that the web slenderness ratio, global slenderness ratio and initial constant axial load ratio influence the capacity of deep I-shaped columns based on detailed finite element analyses of wide flange columns with different boundary conditions. Considering these variables for the four specimens tested, the proposed design guideline equations<sup>10</sup> corroborate the experimental results as they predict an ability to reach 0.04 rad drift without collapse for the subassembly and isolated column tests.

#### 4.5 | Out-of-plane deformation

A motion capture system with sensing marks was used to measure the specimen deformation along the column height. Figure 18(A) shows the web out-of-plane deformation along the column height. When plastic hinges form at the top and bottom ends of the isolated column, both ends of the column displace transversely at large drifts. This behavior is not observed in the subassembly Specimens IC-37-S(R) and IC-49-S because the top end of the first-story column does not form a plastic hinge. Moreover, the magnitude of the flange out-of-plane deformation at the column base is similar in all four specimens, with values around 30 mm at 0.04 rad drift [see Figure 18(B)].

### 5 | NONLINEAR MODELING AND CYCLIC BACKBONE CURVE

For performance-based nonlinear analysis, several documents (e.g.,<sup>21,22,23</sup>) provide guidelines on column modeling. For example, ASCE 41<sup>21</sup> uses the cyclic backbone curve like that shown in Figure 19(A) to model the columns. Based on the elastic stiffness  $K$  and the reduced plastic moment,  $M_y$ , the yield chord rotation,  $\theta_y$ , can be computed. Based on the section compactness and the gravity axial force level, expressions for parameters  $a$ ,  $b$ , and  $c$  are then provided; these parameters are a function of the axial force gravity level, section and member slenderness ratios. When the axial force is less than 50%

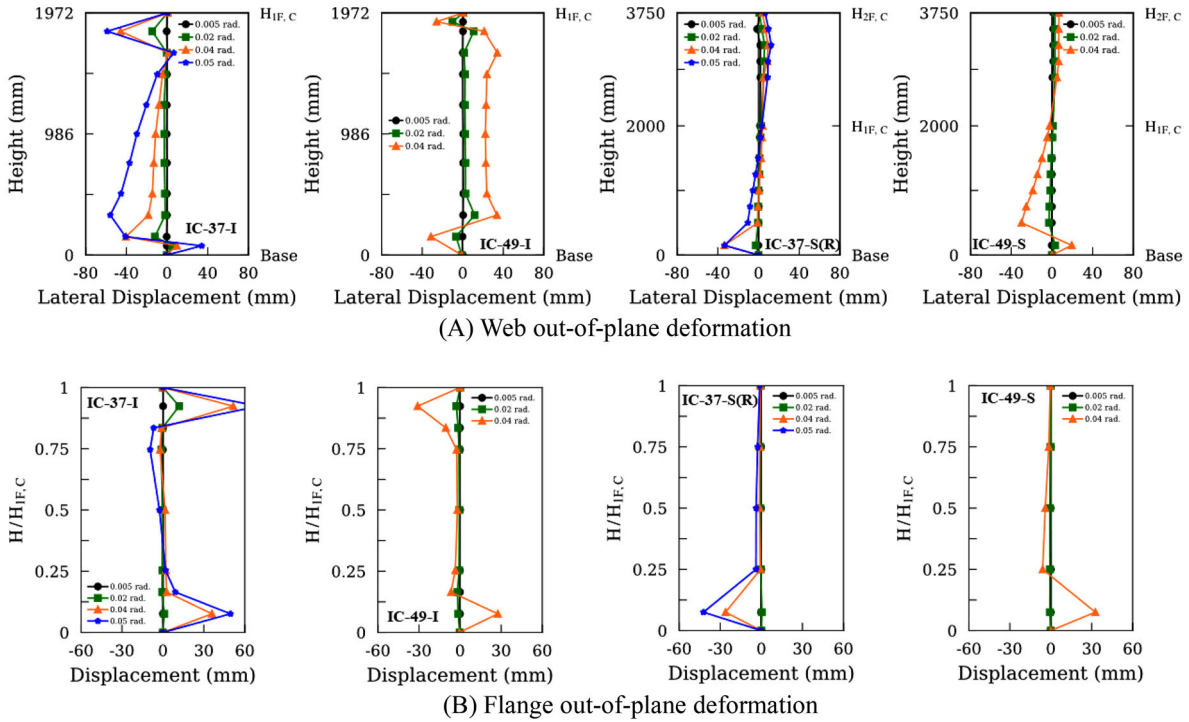


FIGURE 18 Column out-of-plane deformation

of the expected yield force, ASCE 41<sup>21</sup> and NIST<sup>22</sup> use the following elastic flexural stiffness to compute  $\theta_y$  when the point of contra flexural is anticipated to occur at the midspan of the beam or column:

$$K = \frac{6EI_c}{L_c(1 + \eta)} = \frac{K_b K_s}{K_b + K_s} \quad (14)$$

where  $I_c$  is the moment of inertia about the column axis in a direction of bending considered,  $L_c$  is the column length, and  $\eta$  is to account for the effect of shear deformation:

$$\eta = \frac{12EI_c}{L_c^2 G_s A_w} \quad (15)$$

where  $G_s$  is the shear modulus and  $A_w$  is the shear area. The flexural and shear stiffnesses in Equation (14) are  $K_b = 6EI_c/L_c$  and  $K_s = G_s A_w L_c / 2$ , respectively. With the assumption of the location of contra flexural point made by ASCE 41 and NIST, it appears that a comparison can only be made to the test data of isolated column specimens. Since first-story columns in a moment frame generally violate this assumption, yet no guidance is provided by ASCE 41 or NIST, a recommendation will be made on the calculation of  $\theta_y$  when a comparison is made on the subassembly test results.

## 5.1 | Isolated columns

A comparison of the cyclic backbone curves is presented in Figure 19(B) and (C). It is shown that the predictions based on ASCE 41 are very conservative. In particular, the post-peak response [C-D-E in Figure 19(A)] does not resemble the test response and the strength degradation is exaggerated. For Specimen IC-37-I, the NIST prediction is very satisfactory. But the prediction is still conservative for Specimen IC-49-I and the peak strength is underestimated. Ozkula et al.<sup>23</sup> provides an improved prediction of the peak strength for the latter specimen, but the corresponding story drift angle at peak strength is apparently overpredicted.

A comparison of the elastic stiffness, which is needed to compute  $\theta_y$ , is provided in Table 5. Since ASCE 41 and NIST are based on Equations (14) and (15) to compute the elastic flexural stiffness,  $K$ , only ASCE 41 values are listed. The prediction by Ozkula et al. is based on Equations (14) and (15), but a reduction ( $= 1 - P/P_e$ ) is included to reflect the second-order effect,

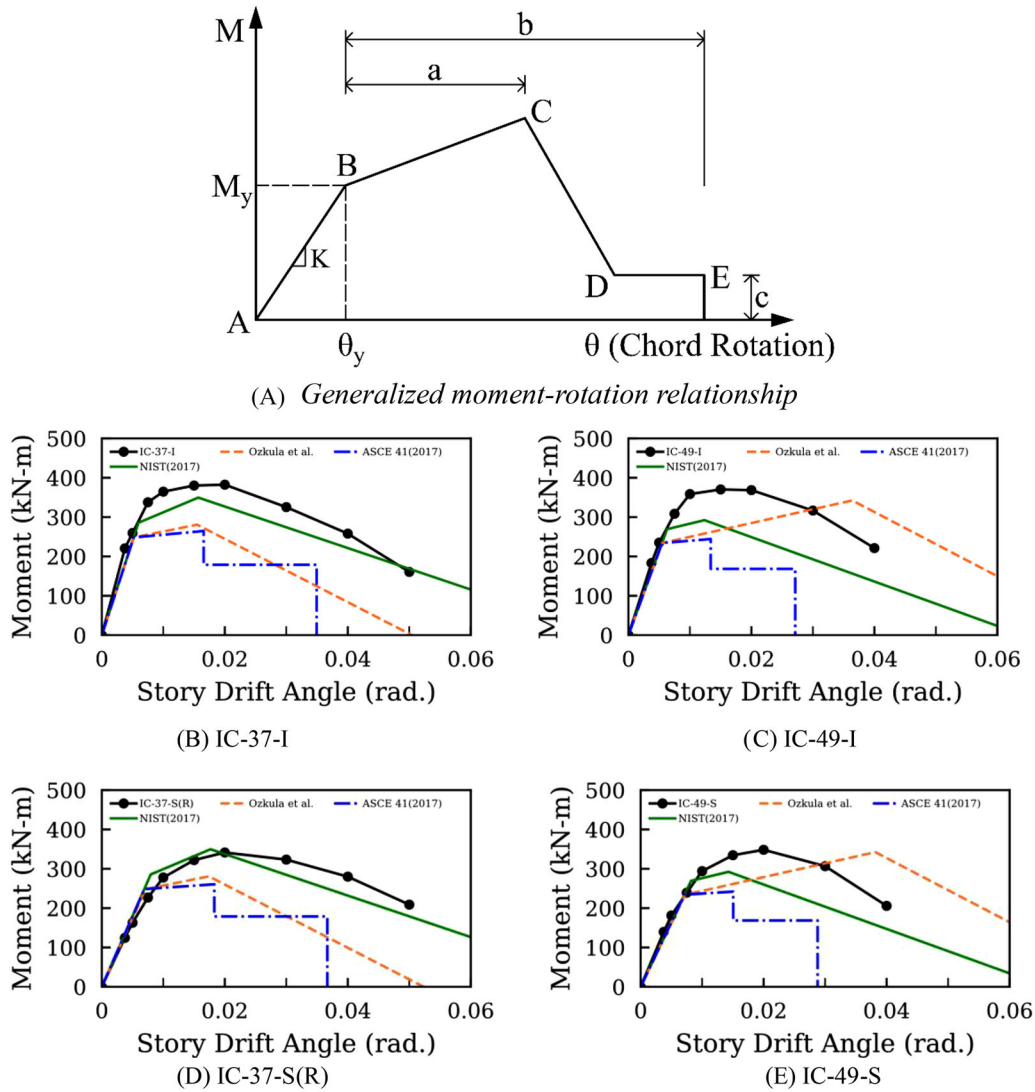


FIGURE 19 Backbone curve comparison of test results and predictions

TABLE 5 Comparison of elastic stiffness K (isolated column)

Specimen	Test (kN-m/rad)	Prediction (kN-m/rad)	
		ASCE 41-17	Ozkula et al.
IC-37-I	50,690	47,929 (5.4%)	47,662 (6%)
IC-49-I	41,818	42,858 (2.3%)	42,649 (2%)

\* Values in parenthesis are error percentage when compared with test value.

where  $P_e$  is the Euler buckling load with the effective length factor  $k = 1$ . The  $(1-P/P_e)$  value is around 0.99, indicating that the flexural stiffness affected by an axial load in the second order analysis is minimal in the isolated specimens.

### 5.2 | Subassemblage first-story columns

It was shown in Figure 16 that, after removing the elastic component, the plastic components of the cyclic backbone curves for both the isolated column and first-story column in a subassemblage are very similar. Since elastic lateral stiffness provided in ASCE 41 is only applicable for fixed-fixed isolated columns, a procedure based on LeMessurier<sup>24</sup> is provided below to calculate the lateral stiffness of any column in a moment frame.



TABLE 6 Elastic stiffness of first-story columns K in subassemblage

Subassemblage	End Condition				Prediction (kN-m/rad)			Test (kN-m/rad)	
	$G_A$	$G_B$	$\beta$	$\alpha$	$K_b^a$	$K_b(1-P/P_e)$	$K_s$	$K$	$K$
IC-37-S(R)	5.5	0.0	4.9	3.62	39,243	38,447	182,154	31,746	26,998
IC-49-S	5.3	0.0	5.0	3.67	38,198	37,468	136,615	29,403	27,551

<sup>a</sup>Values are calculated based on Equation (20).

Use  $G$  to measure the rotational restraint at each end of the column:

$$G = \frac{\sum EI_c/L_c}{\sum EI_b/L_b} = \frac{\sum I_c/L_c}{\sum I_b/L_b} \quad (16)$$

where  $I_b$  is the moment of inertia of the beam,  $L_b$  is the length of the beam. Note that this parameter  $G$  is also used to compute the effective length factor of columns in AISC 360.<sup>25</sup> For a given column shear,  $V$ , moments at end joints A (top end) and B (bottom end) are:

$$M_A = \left[ \frac{G_B + 3}{G_A + G_B + 6} \right] VL_c \quad (17a)$$

$$M_B = \left[ \frac{G_A + 3}{G_A + G_B + 6} \right] VL_c \quad (17b)$$

The ratio between the relative lateral displacement and the column length represents the story drift angle (or chord rotation) and is expressed as follows:

$$\frac{\Delta}{L_c} = \frac{L_c^2}{\beta EI_c} V \quad (18)$$

where  $\beta$  is a factor to account for the elastic end restraints<sup>24</sup>:

$$\beta = \frac{6(G_A + G_B) + 36}{2(G_A + G_B) + G_{AGB} + 3} \quad (19)$$

When both ends are fixed ( $G_A = G_B = 0$ ),  $\beta = 12$  and the solution converges to the fixed-fixed boundary condition. Combining Equations (17b) and (18), the relationship between the moment at the bottom end of the column and the story drift angle is:

$$M_B = \left[ \frac{(G_A + 3)\beta EI_c}{(G_A + G_B + 6)L_c} \right] \left( \frac{\Delta}{L_c} \right) = \left[ \frac{(G_A + 3)\beta}{(G_A + G_B + 6)} \right] \left( \frac{EI_c}{L_c} \right) \left( \frac{\Delta}{L_c} \right) = \alpha \left( \frac{EI_c}{L_c} \right) \left( \frac{\Delta}{L_c} \right) = K_b \left( \frac{\Delta}{L_c} \right) \quad (20)$$

where  $\alpha$  represents a bending coefficient that accounts for the column end restraints (i.e., 6 for the fixed-fixed column boundary condition).

Figure 19(D) and (E) show the backbone curve of the first-story columns in the subassemblages. See Table 6 for the calculation of the elastic stiffness. In determining the  $G$  value for the column base, AISC 360 recommends a value of 1.0 instead of the theoretical value ( $= 0.0$ ). Column base rotation was monitored in this test program. Figure 17(E) shows that the measured rotation was negligibly small, thus justifying the fixed boundary condition ( $G_B = 0$ ). The results showed that the procedure presented above can reasonably predict the elastic stiffness. The corresponding flexural stiffnesses,  $K_b$ , obtained from Equation (20) is  $3.62EI_c/L_c$  and  $3.67EI_c/L_c$  for Specimens IC-37-S(R) and IC-49-S, respectively, by considering neighboring elements at the first-story column top end, which is not  $6EI_c/L_c$  specified for an isolated column with a symmetric double curvature bending.

## 6 | CONCLUSION

Two two-story steel subassemblage frames with a column and beams at two floor levels were tested to evaluate the effect of adjoining members on the cyclic behavior of the first-story steel columns. The column sections satisfied the

compactness limit of highly ductile members specified in AISC 341.<sup>14</sup> The subassemblages (Specimens IC-37-S(R) and IC-49-S) used I-shaped columns, the difference being that the web width-thickness ratio of the latter (49) was higher than that of the former (37). I-shaped beams with Reduced Beam Section (RBS) moment connections were used for all subassemblages. SN490B steel was specified for all the built-up columns and beams. To contrast the behavior of first-story columns in the subassemblage specimens, two isolated columns (Specimens IC-37-I and IC-49-I) with a fixed-fixed boundary condition were also tested so a direct comparison could be made. The following conclusions can be drawn.

1. Both subassemblage specimens experienced plastic hinging at the column base only. The specimens first experienced plastic hinge formation in the RBS regions of the beams, causing the inflection point of the first-story column to move upward. When significant local buckling developed at the column base at and beyond 0.02 rad drift, strength degradation then caused the inflection point to move downward. No yielding or buckling was observed at the top end of the first-story column, although minor out-of-plane deformation was observed at the end of the test due to lateral-torsional buckling of the second-floor beams.
2. Plastic hinging with local buckling was significant at both ends of the isolated column specimens, causing both ends of the column to displace out of plane at drifts larger than 0.03 rad (Figures 13 and 14). While similar behavior for isolated columns was also reported by previous researchers, such out-of-plane deformation was not seen in the subassemblage specimens because only one plastic hinge formed at the column base (Figures 10 and 18).
3. Of the two subassemblage specimens tested, Specimen IC-49-S showed a more significant post-buckling strength degradation of the first-story column as expected due to a larger column web width-thickness ratio [Figures 8(A) and 11(B)]. Testing of the subassemblage specimen further showed that such “significant” strength degradation at the component level was “smeared” at the global response level due to the contribution from other structural members [Figures 5(A) and 11(A)].
4. The behavior of isolated columns and columns in a subassemblage frame was different in several aspects. In addition to the differences in the location of inflection point and out-of-plane deformation mentioned in Items 1 and 2 above, the yield rotation of a first-story column in a subassemblage frame was increased significantly, making the overall rotation capacity also larger. But results from this research showed that the moment-rotation response at the column base in both cases is similar in the inelastic range, i.e., the inelastic deformation capacity is independent of the column top end boundary condition [Figure 16(E) and (F)].
5. Based on LeMessurier,<sup>24</sup> a closed-form procedure was developed to evaluate the elastic lateral stiffness of a first-story column with rotational restraint at both ends in a multistory frame. This elastic stiffness forms the elastic portion of the cyclic backbone curve of a first-story column. When combined with the second-order effect, this proposed procedure provides a very good correlation with the experimentally determined elastic lateral stiffness for the two subassemblage specimens [Figure 19(D) and (E)].

Note that a concrete slab was not incorporated in the subassemblage tests. Further research is needed to evaluate the degree of rotational restraint that the concrete slab would contribute to the top end of the first-story columns.

## ACKNOWLEDGEMENTS

The cooperative research project among NCREC, National Taiwan University, University of California, San Diego, and University of Michigan, Ann Arbor is supported by the Ministry of Science and Technology (award 108-2625-M-002-003), Taiwan. Additional support is provided by the financial assistance award 70NANB171TZ91 from the U.S. Department of Commerce, National Institute of Standards and Technology. Any opinions, findings, conclusions, and recommendations expressed in this paper are those of the authors and do not necessarily reflect the views of the sponsor.

## DATA AVAILABILITY STATEMENT

The data that support the findings of this study are available from the corresponding author upon reasonable request.

## ORCID

Chung-Che Chou  <https://orcid.org/0000-0002-6791-3790>

Gulen Ozkula  <https://orcid.org/0000-0002-1947-6362>

## REFERENCES

1. Wu TY, El-Tawil S, McCormick JP. Seismic collapse response of steel moment frames with deep columns. *J Struct Eng ASCE*. 2018;144(9):04018145.
2. Varma AH, Ricles JM, Sause R, Lu LW. Experimental behavior of high strength square concrete-filled steel tube beam-columns. *J Struct Eng ASCE*. 2002;128(3):309-318.
3. Leon RT, Kim DK, Hajjar JF. Limit state response of composite columns and beam-columns Part 1: formulation of design provisions for the 2005 AISC specification. *Eng J*. 2007(4th):341-358.
4. Newell J, Uang CM. Cyclic behavior of steel wide-flange columns subjected to large drift. *J Struct Eng ASCE*. 2008;134(8):1334-1342.
5. Lignos DG, Cravero J, Elkady A. Experimental investigation of the hysteretic behavior of wide-flange steel columns under high axial load and lateral drift demands. Proc. of 11th Pacific Structural Steel Conf, Shanghai, China; 2016.
6. Fogarty J, El-Tawil S. Collapse resistance of steel columns under combined axial and lateral loading. *J Struct Eng ASCE*. 2016;142(1):04015091.
7. Elkady A, Lignos DG. Full-scale testing of deep wide-flange steel columns under multiaxis cyclic loading: loading sequence, boundary effects, and lateral stability bracing force demands. *J Struct Eng ASCE*. 2018;144(2):04017189.
8. Chou CC, Wu SC. Cyclic lateral load test and finite element analysis of high-strength concrete-filled steel box columns under high axial compression. *Eng Struct*. 2019;189:89-99.
9. Chou CC, Chen GW. Lateral cyclic testing and backbone curve development of high-strength steel built-up box columns under axial compression. *Eng Struct*. 2020;223:111147.
10. Wu TU, El-Tawil S, McCormick JP. Highly ductile limits for deep steel columns. *J Struct Eng ASCE*. 2018;144(4):04018016.
11. Suita K, Yamada S, Tada M, Kasai K, Matsuoka Y, Shimada Y, (2008). Collapse experiment on four-story steel moment frame: part 2. Proceeding of the 14th World Conference on Earthquake Engineering, Beijing, China.
12. Del Carpio M, Mosqueda G, Hashemi MJ. Large-scale hybrid simulation of a steel moment frame building structure through collapse. *J Struct Eng*. 2015;142(1):04015086.
13. Hashemi MJ, Mosqueda G. Innovative substructuring technique for hybrid simulation of multi-story buildings through collapse. *Earthq Eng Struct Dyn*. 2014;43(14):2059-2074.
14. Chou CC, Lin TH, Lai YC, et al. US-Taiwan collaborative research on steel column through cyclic testing of two-story subassemblages. 17th World Conference on Earthquake Engineering, Paper No. C4352 (2i-0213), Sendai, Japan; 2020.
15. Lai YC. In: Chou C C, ed. *H-Shaped Steel Columns under Cyclic Loading: Two-Story Subassemblage and Member Test*. Thesis Advisor. Department of Civil Engineering, National Taiwan University; 2020.
16. Lin TH, Chou CC. High-strength steel deep H-shaped and box columns under proposed near-fault and post-earthquake loadings. *Thin-Walled Struct*. 2022;172:108892.
17. ANSI, AISC 341-16. *Seismic Provisions for Structural Steel Buildings*. AISC; 2016.
18. ANSI, AISC 358-16. *Prequalified Connections for Special and Intermediate Steel Moment Frames for Seismic Applications*. Chicago: AISC; 2016.
19. Ozkula G, Harris J, Uang CM. Observations from cyclic tests on deep, wide-flange beam-columns. *AISC Eng J*. 2017;54(1):45-61.
20. Reynolds M, Uang CM. Economical weld details and design for continuity and doubler plates in steel special moment frames. *J Struct Eng ASCE*. 2022;148(1):04021246.
21. ASCE. *Seismic Evaluation and Retrofit of Existing Buildings*. ASCE/SEI 41-17. American Society of Civil Engineers; 2017.
22. NIST. *Guidelines for Nonlinear Structural Analysis for Design of buildings: Part IIA – Steel Moment Frames*. NIST GCR 17-917-46v2. National Institute of Standards and Technology; 2017.
23. Ozkula G, Harris J, Uang CM. *Cyclic Backbone Curves for Steel Wide-Flange Columns: A Numerical Study*. EUROSTEEL; 2017:3365-3374.
24. LeMessurier WM. A practical method of second order analysis: part 2-rigid frames. *Eng J*. 1977;Second Quarter:49-96.
25. ANSI, AISC 360-16. *Specification for Structural Steel Buildings*. AISC; 2016.

**How to cite this article:** Chou C-C, Lai Y-C, Xiong H-C, et al. Effect of boundary condition on the cyclic response of I-shaped steel columns: Two-story subassemblage versus isolated column tests. *Earthquake Engng Struct Dyn*. 2022;1-22. <https://doi.org/10.1002/eqe.3730>